A Universal Filter Approximation of Edge Diffraction for Geometrical Acoustics

Christoph Kirsch and Stephan D. Ewert

***Abstract*—Sound propagation in urban and indoor environments often involves diffraction at corners, finite objects and openings, resulting in perceptually relevant frequency-dependent attenuation. Geometrical acoustics (GA) has become a de-facto standard for the prediction and simulation of sound propagation and real-time virtual acoustics, including effects of edge diffraction. However, methods to account for edge diffraction often assume infinite edges, such as the uniform theory of diffraction, or are computationally involved, such as the Biot-Tolstoy-Medwin-Svensson (BTMS) method. Particularly for interactive auralization, an efficient approximation of edge diffraction is desirable. Here, an extension of GA to account for diffraction with simple-to-derive parameters and a time-domain recursive filter implementation is suggested. This universal diffraction filter approximation (UDFA) describes diffraction from infinite and finite wedges using a combination of first-order and (fractional) half-order low-pass filters to account for the frequency-dependent attenuation of the diffracted incident and reflected sound field. The physically-based UDFA exactly matches asymptotic solutions for infinite wedges and provides approximations for finite wedges. It is demonstrated that first-order diffraction from flat finite objects like a plate or an aperture can be described by combining the filters for each edge. To account for effects of higher-order diffraction, an additional heuristic filter extension is suggested.**

***Index Terms*—Diffraction, room acoustics, virtual acoustics, virtual reality, scattering.**

I. Introduction

THE wave properties of sound cause diffraction at edges and objects, with perceptually notable or specifically desired frequency-dependent attenuation, e.g., for sound barriers [1]. When the direct sound path is occluded, typically a low-pass characteristic is observed. Unlike in vision, where an occluded light source abruptly becomes invisible when the receiver enters the shadow zone, diffracted parts of the sound are still audible and "bend" around the edge. Effects of diffraction are highly relevant in the context of room acoustics simulation [2], [3], [4], [5] and in (interactive) virtual acoustic environments (VAEs) with dynamic sound sources and receivers. Besides applications in architectural acoustics [6] and archaeoacoustics [7], such VAEs have recently gained interest for hearing research and development of signal processing algorithms aiming at ecological validity [8], [9], [10] or a high degree of perceptual plausibility [11].

For acoustics simulation of in indoor and urban outdoor environments, geometrical acoustics (GA), assuming ray-like sound propagation, offers advantages with regard computational complexity [12], [13], [14] and have become a de-facto standard. Effects of diffraction can be included in GA by constructing sound ray propagation paths involving "bending" at edges [15] like building or room corners, or at the boundaries of smaller objects, like boards or plates [16], [17], [18], [19].

Generally, descriptions of diffraction date back to Huygens in the 17th century. In optics, a solution for diffraction at a rigid or compliant half-plane has been developed by [20] and a solution exists also for diffraction at a wedge with given face impedances [21]. The concept of edge diffracted rays in geometrical optics was described in the geometrical theory of diffraction (GTD) [22], considering the incident and reflected diffracted field at straight and curved edges. GTD offers only limited validity in particular geometrical conditions [23], [24]. Incremental improvements were made to describe diffraction based on rays with the uniform asymptotic theory of electromagnetic diffraction [25]. The uniform theory of diffraction (UTD) [26] has been established as an asymptotic high-frequency solution for diffraction of electromagnetic waves. Similar asymptotic solutions [27], [28], [29] have been derived for acoustic diffraction. Diffraction at a nearly rigid wedge was considered in [30], and in [28] limiting cases with the sound source near the diffracting edge were investigated. An independent approach to an asymptotic solution was proposed in [31], [32]. Different analytical solutions are reviewed in [24], and asymptotic approaches are compared in [33]. To overcome limitations of GTD in terms of discontinuities and shape of the diffracting edge, the incremental theory of diffraction [34] has been suggested, calculating the diffracted field as a superposition of incremental field contributions from points along the edge. The incremental model has been further developed in [35] for applications in ultrasonic nondestructive testing.

For simplification, infinite edges have often been considered in acoustics, e.g., as an approximation of corners in rooms terminated by reflecting, perpendicular boundaries or of sufficiently wide (sound) barriers, however, also for finite edges [5], [36]. The computational effort of the involved calculations can be reduced by using approximations (e.g., [37] for the Fresnel terms in UTD) or by evaluating a diffraction solution

Manuscript received 22 June 2022; revised 14 February 2023; accepted 20 March 2023. Date of publication 5 April 2023; date of current version 28 April 2023. This work was supported by the Deutsche Forschungsgemeinschaft under DFG Grant 352015383–SFB 1330 C5. The associate editor coordinating the review of this manuscript and approving it for publication was Prof. Stefan Bilbao. *(Corresponding author: Christoph Kirsch.)*

The authors are with the Medizinische Physik and Cluster of Excellence Hearing4All, Carl von Ossietzky Universität, 26129 Oldenburg, Germany (e-mail: christoph.kirsch@uol.de; stephan.ewert@uol.de).

Digital Object Identifier 10.1109/TASLP.2023.3264737

only at a low frequency resolution. A considerably simpler empirical approximation for frequency-dependent attenuation of wide sound barriers was suggested in [38]. For the directive line source model [39], [40], empirical expressions have been derived that are faster to calculate and can also represent absorbing wedges [1].

Time-, and later frequency-domain solutions were presented based on the concept of secondary sources located along the edge [41], [42], reformulating and extending earlier (exact) time-domain solutions [43], [44] to line integrals along the physical edge. The line integral formulation, referred to as BTMS, also makes finite edges and consequently objects composed thereof easier treatable, including higher-order diffraction. An integral formulation that enables higher-order diffraction modeling for convex objects at reasonable computation times was introduced in [45]. Also, efforts were made to minimize the computation time when evaluating edge diffraction with BTMS [46], [47].

An important simplification for interactive VAEs is to consider effects of diffraction only in the shadow zone, where the direct sound GA component is obstructed, and perceptual effects can be considered most prominent. In this case, it is desired that the effect of diffraction disappears at the shadow boundary and asymptotes against unity gain [16], [36]. A computationally efficient, parametric infinite impulse response (IIR) filter approximation of diffraction effects for the shadow zone based on the infinite knife edge was proposed in [48]. In general, such low-order IIR filters (also see, e.g., [2] for a warped IIR design) offer high computational efficiency and the ability to conveniently interpolate filter coefficients in time-variant geometrical conditions. Parametric IIR filters have also been optimized in [49] by a machine learning approach to model diffraction of a flat, finite object, without restrictions to the shadow zone.

Overall, several solutions for interactive diffraction simulation exist, e.g., approximating the infinite edge frequency response in the shadow region using bandpass bands [36], or coarsely approximating the average filter characteristic for prototypical object shapes [19]. However, no scalable filter solution exists, suited to adjust the acoustic level of detail for simulating diffraction. Such a solution is required to i) investigate the perceptually required level of detail, as well as to ii) assess the level of detail required for the function of (ear-level) signal processing algorithms in ecologically valid communication and conferencing scenarios.

Recently, [50] suggested a parametric filter representation of diffraction at infinite and finite wedges based on the asymptotic solutions [26], [27], [29], and including an approximation of the exact BTMS solution. While this filter representation offers a physically-based, fast and accurate theoretical description of first-order diffraction at arbitrary wedges for any geometric arrangement of source, receiver, and wedge, no applicable IIR filters were derived. Furthermore, the suggested solution for finite wedges, involving time-domain truncation or frequency domain convolution with the according sinc function, is not well suited for real-time applications. Finally, it remains unclear how well diffraction at finite objects and apertures (e.g., doors) can be accounted for by combining the filter representation for multiple edges.

Here, a physically-based filter method is proposed to universally account for diffraction from infinite and finite wedges, as well as from flat finite objects composed of edges. The suggested universal diffraction filter approximation (UDFA) uses a combination of first-order and (fractional) half-order low-pass filters to account for the diffracted sound field for an arbitrary geometrical arrangement of source, receiver, and wedge. UDFA characterizes the diffracted sound by filter parameters, derived from simple expressions which are well suited for real-time applications, and is extendable using different underlying diffraction solutions. In comparison to the (reference) BTMS solution and acoustic measurements, it is demonstrated that UDFA accounts well for first-order diffraction from infinite and finite edges, as well as from finite flat rigid objects like a plates and apertures. A parametric design for recursive (IIR) filters with scalable precision is proposed, enabling straight forward interpolation of the filter coefficients in time-variant geometrical conditions in VAEs.

The remainder of this paper is structured as follows: Section II outlines the underlying filter representation [50] for infinite wedges and derives an exact solution for the heuristic filter approximation in [48]. Section III derives the filter approximation for finite wedges. In Section IV, an IIR filter implementation of the required half-order low-pass filters is proposed. Section V provides an error and computation time evaluation. Section VI applies UDFA to finite objects composed of multiple edges and proposes a heuristic extension to approximate higher-order diffraction effects. Finally, Section VII discusses the results, and Section VIII concludes the paper.

II. Approximation of Infinite Wedge Diffraction

A rigid infinite wedge along the z-axis of a cylindrical coordinate system is considered, comprised of two intersecting planes as shown in Fig. 1. The source (blue cross) is arbitrarily assumed to be closer to either wedge plane, $P_{\mathrm{e,s}}$, than the receiver (red circle), reflecting reciprocity of the problem. $P_{\mathrm{e,s}}$ serves as the reference to all azimuth angles θ. The second wedge plane, $P_{\mathrm{e,r}}$, is located at the exterior wedge angle θ_{w}. Source and receiver are located in the planes P_{s} and P_{r} with axial coordinates z_{s}, z_{r}, radial distances r_{s}, r_{r}, and azimuth angles θ_{s}, θ_{r}, respectively. At the apex point z_{a}, the incidence angle φ between edge and vector to the source in plane P_{s} is equal to the angle between edge and vector to the receiver in plane P_{r}. The distances between source and receiver and the apex point z_{a} are d_{s} and d_{r}, respectively.

Past the shadow boundary (SB) at $\theta_{\mathrm{s}} + \pi$, the source becomes invisible to the receiver and only the diffracted field exists (referred to as shadow zone, SZ). In addition to the incident GA sound field existing in the "view" or "illuminated" zone (VZ), a reflected GA sound field additionally exists in the reflection zone (RZ), separated by the reflection boundary (RB) at $\pi - \theta_{\mathrm{s}}$ from the view zone. Depending on exterior wedge angle θ_{w} and source plane angle θ_{s}, up to two reflection zones may exist (if the SB is located inside wedge), i) at angles $< \pi - \theta_{\mathrm{s}}$, and ii) at angles $> 2\theta_{\mathrm{w}} - \pi - \theta_{\mathrm{s}}$. Hereby, a RB represents the SB for an image source in either wedge plane. A diffracted transmission path with bending angle $\theta_{\mathrm{b}} = \theta_{\mathrm{r}} \ - \pi - \theta_{\mathrm{s}}$ between the source

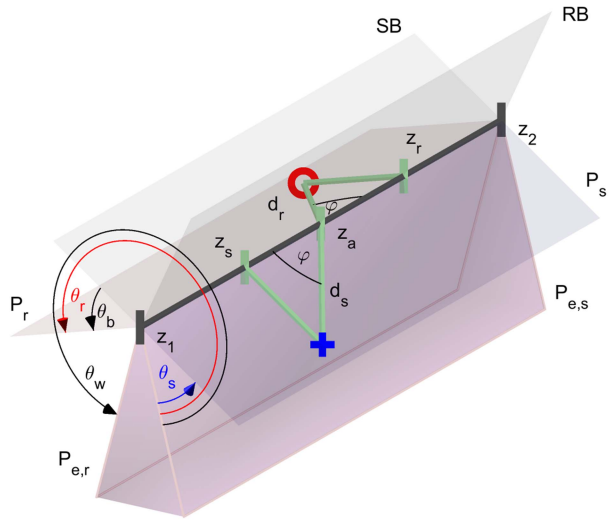

Fig. 1. A wedge is located on the longitudinal z-axis of a cylindrical coordinate system, spanning from z_1 to z_2, or $\pm\infty$ in case of an infinite wedge. The wedge is formed by two intersecting planes, $P_{\mathrm{e,s}}$ and $P_{\mathrm{e,r}}$ facing source (blue cross) and receiver (red circle), located in the planes P_{s} and P_{r} (grey) at an angle φ to the edge at apex point z_{a}. The planes P_{s} and P_{r} are located at angles θ_{s} and θ_{r}, with all azimuth angles referenced to $P_{\mathrm{e,s}}$. The exterior wedge angle is referred to as θ_{w}. SB and RB denote the shadow and reflection boundary, respectively. The angle between the SB at $\theta_{\mathrm{s}}+\pi$ and P_{r} is referred to as bending angle θ_{b}.

and receiver can be constructed using the apex point z_{a} on the axial dimension along the edge, which serves as a center node [42].

To describe edge diffraction, the exact BTMS [41] and the asymptotic UTD [26] and Pierce [27], [29] solutions use up to four diffraction terms. These terms exhibit discontinuities at the (real and virtual) shadow and reflection boundaries, where the GA component itself experiences a discontinuity [51]. The combination of the incident, reflected, and diffracted components results in a continuous sound field.

A. Filter Representation of Wedge Diffraction

In [50], a two-term filter representation (representing the incident and reflected diffracted field), based on the asymptotic solution in [27], [29] was derived, forming the basis of the here suggested UDFA:

The asymptotic two-term solution for diffraction by an infinite wedge in [27], [29] is given by

$$p_D = \frac{\mathrm{e}^{-jkd}}{d}\,\frac{\mathrm{e}^{-j\pi/4}}{\sqrt{2}}\left(G_{\nu+}A_D\left(X_+\right)+G_{\nu-}A_D\left(X_-\right)\right), \quad (1)$$

with the wave number $k=2\pi f/c$, the distance between source and receiver over the apex point $d=d_{\mathrm{s}}+d_{\mathrm{r}}$ and speed of sound c. The two diffraction functions $A_D(X_\pm)=\mathrm{sign}(X_\pm)[f(|X_\pm|)-jg(|X_\pm|)]$ are composed of auxiliary Fresnel functions. The subscripts $\pm$ indicate that the respective functions are evaluated for two angles, $X_+=X\left(\theta_+\right)=X(\theta_{\mathrm{r}}+\theta_{\mathrm{s}})$ and $X_-=X\ \left(\theta_-\right)=X(\theta_{\mathrm{r}}-\theta_{\mathrm{s}})$. The diffraction functions $A_D(X_\pm)$ can be represented by half-order low-pass filters $H_\pm$ that asymptote against a $1/\sqrt{f}$ slope (-3 dB/octave) [50]:

$$p_D=\frac{\mathrm{e}^{-jkd}}{2d}\left(G_{\nu+}\mathrm{sign}\left(\theta_+-\pi\right)H_+ + G_{\nu-}\mathrm{sign}\left(\theta_--\pi\right)H_-\right). \quad (2)$$

The gain $G_{\nu\pm}\left(\theta\right)=G_\nu\ \left(\theta_\pm\right)$ depends on the angular positions of source and receiver and the exterior wedge index $\nu=\pi/\theta_{\mathrm{w}}$:

$$G_{\nu\pm}(\theta)=\frac{\sin\left(\nu\pi\right)}{\left(1-\cos\left(\nu\pi\right)\cos\left(\nu\theta\right)\right)^{1/2}}\ . \quad (3)$$

For integer ν, the diffracted field disappears. For knife edges, ν equals $1/2$, resulting in $G_{\nu\pm}\left(\theta\right)=1$. The cutoff frequencies $f_{\mathrm{c}\pm}$ of the low-pass filters $H_\pm$ for the incident and reflection component can be derived from (1) by assuming a fixed value of $X_\pm=\sqrt{2}/\pi$:

$$f_{\mathrm{c}\pm}(\theta)=\frac{2c}{\pi^2 d^*\sin^2(\varphi)}\left[N_\nu\left(\theta\right)\right]^2. \quad (4)$$

Here $d^*=2d_{\mathrm{s}}d_{\mathrm{r}}/d$ is the characteristic distance and

$$N_{\nu\pm}(\theta)=\frac{\nu\sqrt{1-\cos\left(\nu\pi\right)\ \cos\left(\nu\theta\right)}}{\cos\left(\nu\pi\right)-\cos\left(\nu\theta\right)}\ , \quad (5)$$

expresses the dependency of $f_{\mathrm{c}\pm}$ on the source and receiver angles and the exterior wedge index ν.

The low-pass characteristic of the diffraction function A_D in (1) can be approximated with a maximum magnitude error of about ±0.1 dB and maximum phase error of about $\pm1^\circ$ by a modified fractional-order low-pass filter [50]:

$$H(f)=\left(\left(jf/f_{\mathrm{c}}\right)^{2/b}+\left(jf/Qf_{\mathrm{c}}\right)^{1/b^r}+1\right)^{-\alpha b/2}, \quad (6)$$

where $\alpha=0.5$ is the fractional filter order, and the parameters $b=1.44, Q=0.2$, and $r=1.6$ provide a smooth roll-off around the cutoff frequency.

B. Two- and Single-Term Approximation

Generally, the above described two-term solution [50] is used "as is" in UDFA. The use of two terms results in a good approximation of wedges with interior angles $\leq\pi/2$ [37], [50], thus covering the relevant cases of knife edges (approximating thin screens and plates) and of typical square wedges in buildings and man-made structures. Particularly for knife edges, the two-term solution is sufficient, given that the four terms in BMTS and UTD reduce to two filters in this case [50]. Otherwise, UDFA may alternatively use the (four) filter representations [50] of BTMS or UTD to extend the application range. Based on Fig. 4 in [37], we recommended UTD as basis for UDFA if interior wedge angles $>2\pi/3$ are in the focus.

As a simplification, diffraction might only be considered in the shadow zone in UDFA. To ensure a smooth transition to the GA direct sound component, unity gain at the shadow boundary can be achieved by using a single filter (see, e.g., [48] for a heuristically derived expression). The exact cutoff frequency for a single low-pass filter with unity gain at DC and asymptotically matching the two-term filter representation (2), (3), (4), can be

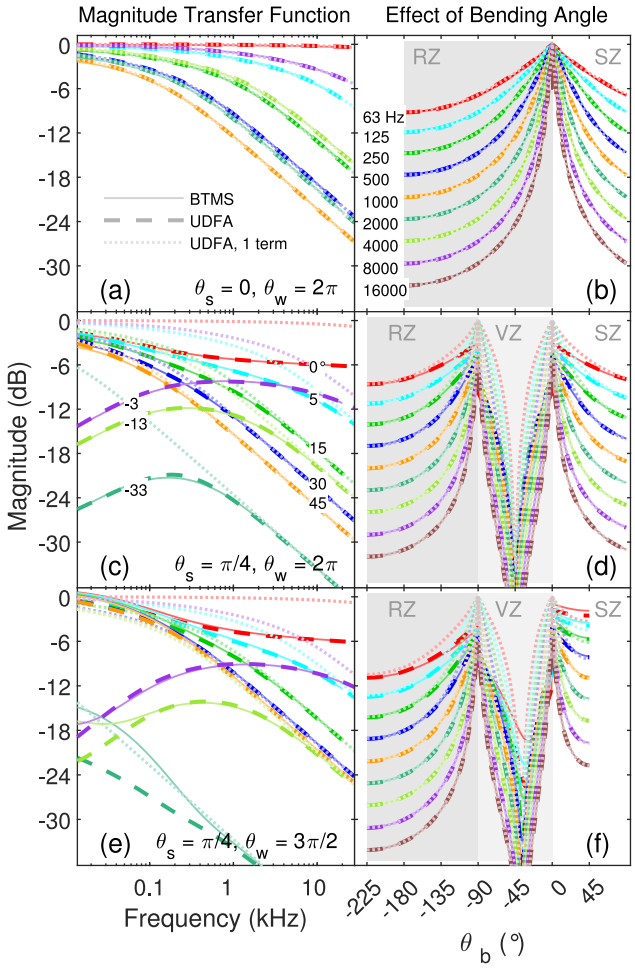

Fig. 2. Reference BTMS wedge diffraction magnitude transfer functions (solid) and UDFA using the two-term (dashed) and single-term approximation (dotted, faint), normalized to path length $d_\mathrm{s} + d_\mathrm{r}$ for different bending angles θ_b over frequency (left column), and for different frequencies over bending angle θ_b (right column). Bending angles are indicated in degrees for convenience. The shadow, view, and reflection zone (SZ, VZ, RZ) are indicated by shaded areas in the right column. Geometrical parameters: $d_\mathrm{s} = d_\mathrm{r} = 2$ m, $\varphi = \pi/2$. Top row: $\theta_\mathrm{s} = 0, \theta_\mathrm{w} = 2\pi$; middle row: $\theta_\mathrm{s} = \pi/4, \theta_\mathrm{w} = 2\pi$; bottom row: $\theta_\mathrm{s} = \pi/4, \theta_\mathrm{w} = 3\pi/2$.

derived as

$$f_{\mathrm{c,single}} = \left(\frac{G_{\nu-}\sqrt{f_{\mathrm{c}-}} + G_{\nu+}\sqrt{f_{\mathrm{c}+}}}{2} \right)^2 \tag{7}$$

$$= \frac{c(\nu \sin(\nu\pi))^2}{2\pi^2 d^* \sin^2(\varphi)} \left(\sum_{\pm} \frac{\mathrm{sign}(\theta_\pm - \pi)}{|\cos(\nu\pi) - \cos(\nu\theta_\pm)|} \right)^2. \tag{8}$$

For a knife edge with the source or receiver located in one of the wedge planes, the shadow- and reflection boundary are coplanar, and this single-term approximation becomes identical to the two-term solution, given that $f_{c-} = f_{c+}$ with $\theta_- = \theta_+$. Here, the simplest expression [50] can be applied in UDFA similar to [48], using the bending angle θ_b:

$$f_{\mathrm{c,single,k},0} = \frac{c}{\pi^2 d^* (1 - \cos(\theta_\mathrm{b})) \sin^2(\varphi)}. \tag{9}$$

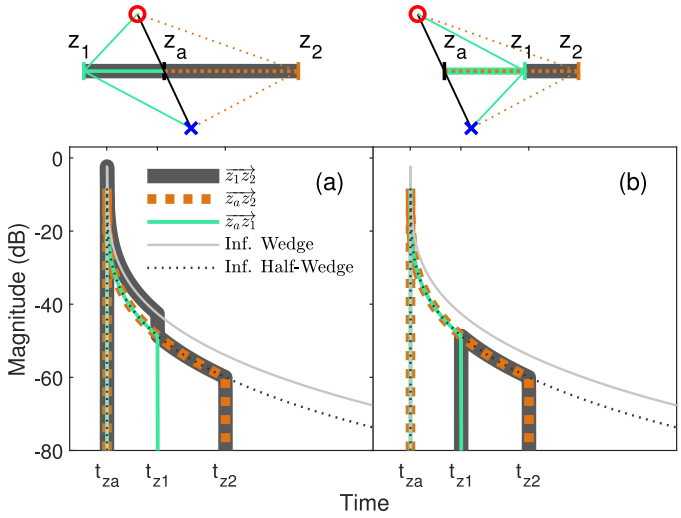

Fig. 3. Paths at finite wedges (2D projection of P_s and P_r, top row), and the corresponding schematic impulse responses (bottom row). Source and receiver are indicated by the cross and the circle. On the left-hand side, the apex point is placed off-center within the wedge. On the right-hand side, the (virtual) apex point is located outside the physical wedge. There are two different path lengths across the edge corner points z_1 and z_2. Contributions to the finite-wedge impulse response (thick, dark grey) by the two half wedges $\overrightarrow{z_1 z_a}$ and $\overrightarrow{z_a z_2}$ are shown as green solid and orange dotted traces. The thin solid trace represents the diffraction impulse response of an infinite wedge and the thin dotted trace represents that of an infinite half wedge extending to one side of z_a.

C. Comparison to the BTMS Solution

Fig. 2 shows the results of the two-term (2) and single-term approximation (7) as bold dashed and faint dotted lines, respectively, in comparison to the BTMS reference (thin, solid) for a knife and square wedge as examples. The diffracted sound pressure is normalized to the length of the diffraction path d between source and receiver. The left panels show the magnitude transfer functions for selected bending angles. The right panels show the magnitude transfer functions at selected frequencies as a function of bending angle. In the top row, the source is located in one of the planes of a knife edge ($\theta_\mathrm{s} = 0, \quad \theta_\mathrm{w} = 2\pi$). Here, the single- and the two-term approximation are identical. Both exactly represent the asymptotic diffraction solution in this case, virtually matching the reference. All diffraction transfer functions are low-pass shaped, with increasing cutoff frequencies for decreasing bending angles.

In the middle row, the source is located outside the knife edge ($\theta_\mathrm{s} = \pi/4, \ \theta_\mathrm{w} = 2\pi$). Again, the two-term approximation closely matches the reference. The single-term approximation deviates from the reference at small bending angles ($< 15°$) inside the shadow and reflection zone. Large deviations also occur at low frequencies in the view zone, where the reference exhibits a band-pass behavior (purple and green traces in panel c).

In the bottom row, results for a square wedge with the source outside the wedge planes are shown ($\theta_\mathrm{s} = \pi/4, \quad \theta_\mathrm{w} = 3\pi/2$). The two-term approximation shows a good agreement with the reference above 200 Hz, except in the view zone. Here, the asymptotic behavior is reached only at increasing frequencies as the angle is approached, at which the components H_+ and

H_- cancel (in this example: at $\theta_\mathrm{b} = -45°$) and the magnitude of diffracted sound drastically decreases. For the single term approximation, errors at low frequencies are superimposed with errors near the zone boundaries and in the view zone, resulting in a reasonable approximation only sufficiently far within the shadow- and reflection zone. Panel (f) illustrates that, despite the deviations observed in the view zone, the single-term approximation still asymptotes the reference otherwise.

In summary, the two-term approximation results in an excellent match for knife edges, reflecting the validity of the underlying asymptotic solution for this case. For the square wedge, a good approximation is achieved. Increasing deviations to the reference are only observed at low frequencies in the view zone, where the diffracted field is generally small. A quantitative error analysis including other wedge angles is provided in Section V. The single-term approximation delivers reasonable results, when diffraction is considered only in the shadow or reflection zone.

III. Approximation of Finite Wedge Diffraction

In the following, we consider a finite wedge of length L with the end points z_1 and z_2, and define $z_1 = -L/2$ and $z_2 = L/2$. Fig. 1 shows a specific case in which the apex point is in the center of the finite wedge ($z_a = 0$). In general, the apex point can be located anywhere within the physical edge or outside (referred to as virtual apex point). We review properties of finite wedge diffraction in the time domain and derive a filter approximation. For (virtual) apex point locations far outside the physical edge ($|z_a| \gg L/2$), a further simplification is proposed and a combined approach for any apex point location is suggested. As for the infinite edge, BTMS [41] serves as a reference.

A. Finite Half Wedges

Infinite wedges can be conceptualized as consisting of two infinite half wedges, extending to either side of the apex point, with a diffraction impulse response (IR) equal to half of the total infinite wedge IR. Accordingly, finite wedges can be assumed to be composed of two finite half wedges, each spanning from the apex point to one of the wedge corner points, if the apex point is located within the physical edge (see geometrical depiction in the top left of Fig. 3). The diffraction IR by a finite half wedge is a truncated version of the infinite half wedge IR, using the travel times t_{z1}, t_{z2} from source to receiver via the respective corner points z_1, z_2 (see also [44]). The depiction of the finite wedge IR in Fig. 3(a) (see also [41], their Fig. 3) shows that the initial part of the IR (dark grey; starting at t_{za}, corresponding to the path over the apex point) is identical to infinite wedge (light grey). At t_{z1}, corresponding to the edge corner point closest to the apex point, a jump to 1/2 of the infinite IR can be observed. After t_{z2}, corresponding to the further corner point from the apex point, the IR ends. If a (virtual) apex point z_a is located outside the physical wedge (Fig. 3(b)), the contribution of the shorter (virtual) half wedge to the closer corner point z_1 (green) is subtracted from the contribution of the (partly virtual) longer half wedge (to the farther corner point; orange dotted line), resulting in a cancellation of the initial (virtual) parts of the IR, such that the remaining IR starts at t_{z_1} and ends at t_{z_2} (dark grey trace in Fig. 3(b)).

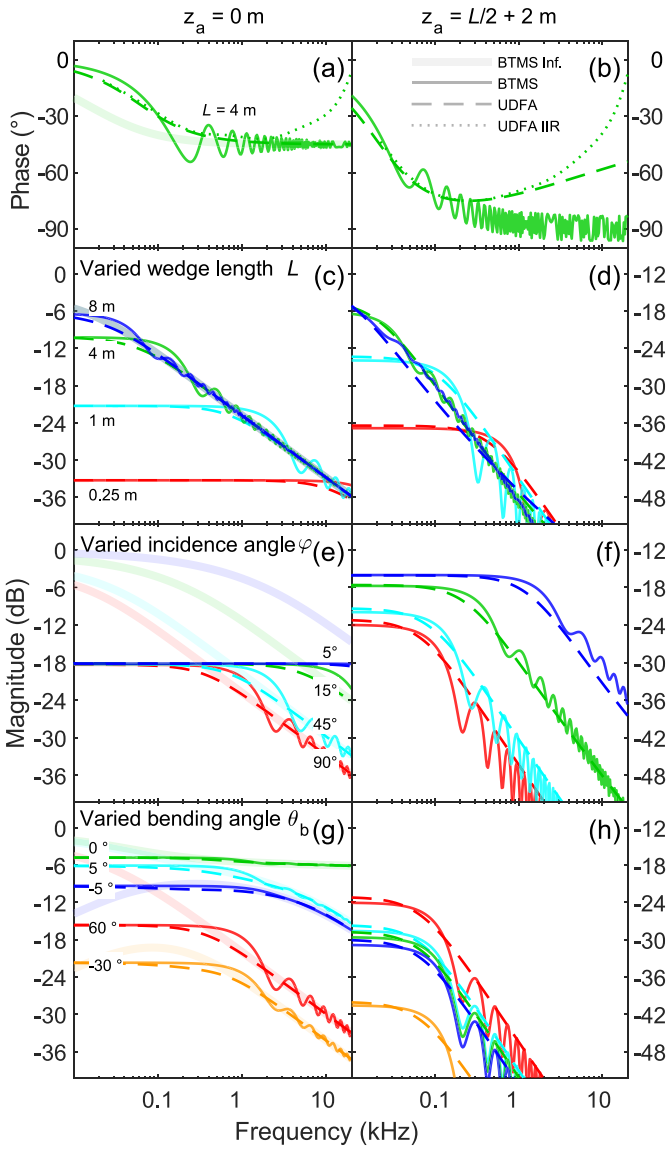

Fig. 4. Edge diffraction phase (top row) and magnitude transfer function (panels c–h) according to BTMS (solid) and UDFA (dashed) normalized to path length $d_\mathrm{s} + d_\mathrm{r}$. Left column: Apex point at the center of the edge, $z_\mathrm{a} = 0$. Thick, faint traces show the corresponding infinite wedge transfer functions. Right column: (Virtual) apex point outside physical the edge, $z_\mathrm{a} = L/2 + 2$ m. (a) And (b): Phase response of a 4-m wedged (same color coding as in c); the dotted line additionally shows the response for the IIR filter approximation). (c) And (d): Varied wedge length L. (e) And (f): Varied incidence angle φ, (g) and (h): Varied bending angle θ_b. Default geometrical parameters: $L = 1.41$ m, $d_\mathrm{s} = d_\mathrm{r} = 4$ m, $\varphi = 90°$, $\theta_\mathrm{s} = \pi/4$, $\theta_\mathrm{b} = \pi/3$, $\theta_\mathrm{w} = 2\pi$.

The spectral properties of finite wedge diffraction are indicated by the solid traces (BTMS) in Fig. 4. The phase response for the example of a 4-m wedge is shown in the top row. The remaining panels show magnitude transfer functions in different configurations. The left column shows symmetric configurations ($z_\mathrm{a} = 0$) as an example for conditions with the apex point located within the physical edge in comparison to the infinite wedge (thick, faint traces). Infinite and finite wedges exhibit the same

asymptotic high-frequency behavior of a half-order low-pass (see solid, colored lines in e.g., Fig. 4(c)) for different wedge lengths). For finite wedges, reduced low-frequency content and spectral ripples occur, resulting from a convolution of the infinite wedge IR with a sinc function, corresponding to the rectangular time domain truncation window [50]. For wedge lengths that are small compared to d^*, the low frequency gain scales linearly with the wedge length (-6 dB per half length). The right column of Fig. 4 shows cases in which the (virtual) apex point is located outside the physical edge at a distance of 2 m from the edge corner. In Fig. 4(d), a phenomenological similar behavior compared to the symmetric case is observed (solid lines, BTMS), with decreasing low-frequency content and an increasing cutoff frequency for shorter wedge lengths L. Ignoring the ripples, the asymptotic high-frequency behavior, however, resembles that of a first-order low-pass with a -6 dB/oct slope in contrast to the -3 dB/oct slope in the symmetric finite (and infinite) case. The different slopes are related to the decay of the diffraction IRs [44], [50]. For apex point locations outside of the wedge, the remaining later part of the half wedge IR decays faster than the initial $1/\sqrt{t}$ decay which causes the -3 dB/oct behavior.

B. Apex Point Inside the Physical Edge

Disregarding spectral ripples, UDFA describes the magnitude response of diffraction from two finite half wedges starting at the apex point by two half-order low-pass transfer functions with a cutoff frequencies $f_{\mathrm{c,fin},1,2}$ and a low-frequency (DC) gains $g_{\mathrm{fin},1,2}$.

The DC gain for each half wedge is obtained from evaluating the integral of the infinite wedge IR $h(t)$ provided in [50] for each of the two diffraction (filter) terms (of the two-term approximation) with the corresponding infinite wedge cutoff frequency f_{c}:

$$g_{\mathrm{fin},1} = \int_0^{t_1} h\,(t)\;dt = \left[\frac{2}{\pi}\;\arctan(\pi\sqrt{2f_{\mathrm{c}}t})\right]_0^{t_{z1}}, \tag{10}$$

Likewise, $g_{\mathrm{fin},2}$ is obtained using t_{z2}. Given that the impulse response of a finite half wedge is a truncated version of a corresponding infinite half wedge, its frequency response converges towards that of the infinite half wedge at high frequencies. The cutoff frequency of an according half-order low-pass filter with $f_{\mathrm{c,fin},1}$ can be derived from $g_{\mathrm{fin},1}$ (for details, see Appendix A):

$$f_{\mathrm{c,fin},1} = \frac{1}{g_{\mathrm{fin},1}^2} f_{\mathrm{c}}. \tag{11}$$

To improve the agreement with the BTMS reference near the cutoff frequency, a heuristically derived adjustment of the parameters b and Q in the transfer function (6) is proposed (omitting the subscripts 1,2):

$$b' = 1 + (b-1)\,g_{\mathrm{fin}}^2 \tag{12a}$$

$$Q' = 0.5 + (Q-0.5)\,g_{\mathrm{fin}}^2, \tag{12b}$$

which results in $b' = b$ for approaching the infinite edge (where $g_{\mathrm{fin}} = 1$), and in $b' = 1$ for small edge lengths. An according behavior is obtained for Q.

Using the two-term approximation for each finite half wedge, the transfer function for finite wedges $H_{\mathrm{fin}}(f)$ is combined as

$$H_{\mathrm{fin}}(f) = \frac{g_{\mathrm{fin},1\pm}H(f_{\mathrm{c}\pm,\mathrm{fin},1}) + g_{\mathrm{fin},2\pm}H(f_{\mathrm{c}\pm,\mathrm{fin},2})}{4} \tag{13}$$

Results are shown in the left column of Fig. 4 for the apex point located in the center of the edge. UDFA (dashed) matches the low frequency gain plateau of the reference and asymptotes the infinite wedge solution for varied edge length in panel (c). The largest deviations between UDFA and the reference appear around the cutoff frequency, where the ripples are not represented. UDFA similarly matches the main characteristics of the reference diffraction function for varied incidence angle φ and varied bending angle θ_{b} as shown in panel (e) and (g) as example configurations. Panel (a) shows that also the phase response (solid) is matched disregarding ripples (dashed). As expected for a half-order, minimum phase system, the phase is 0° in the pass band and converges towards an angle of $-45°$ in the stop band.

C. Apex Point Outside the Physical Edge

For cases in which the (virtual) apex point is located clearly outside the wedge (see solid lines in the right column in Fig. 4 for $z_{\mathrm{a}} = L/2 + 2$ m as an example case), the magnitude transfer function can be efficiently approximated by a single first-order low-pass filter, instead of subtracting transfer functions for both underlying half wedges. The (DC) gain of the low-pass filter results from the truncated segment of the infinite wedge IR determined by paths across both corner points of the wedge, assuming $t_{z_2} > t_{z_1}$:

$$g_{\mathrm{fin,\ off}} = \int_{t_{z1}}^{t_{z2}} h\,(t)\;dt \tag{14}$$

As above, this gain is calculated for the two underlying filter terms. When the distance between the apex point and the closer wedge corner point is sufficiently large in relation to the wedge length, the cutoff frequency of the filter function characterizing an infinite half wedge starting at the closer wedge corner point is small compared to the frequency response of the (rectangular) truncation window. Assuming that the truncation has a dominant influence on the frequency response, the duration $t_{z_2} - t_{z_1}$ of the window determines the cutoff frequency of an according first-order low-pass filter (see Appendix B for details):

$$f_{\mathrm{c,fin,off}} = \frac{1}{\pi\,(t_{z_2} - t_{z_1})}\;. \tag{15}$$

With this filter, UDFA (dashed lines, right column of Fig. 4) outlines the top of the spectral ripples present in the (solid) reference transfer functions. As for the apex point in the center of the edge, the dependence of the diffraction function on wedge length L, incidence angle φ, and bending angle θ_{b} is well covered in panels (d), (f), and (h), respectively. The limitations of determining the cutoff frequency solely from the truncation window duration are apparent in the green and blue traces in panel (d) and (f). Here, a decreasing ripple depth and an underestimation of the cutoff frequency indicate that the truncation is not dominantly determining the transfer functions, violating

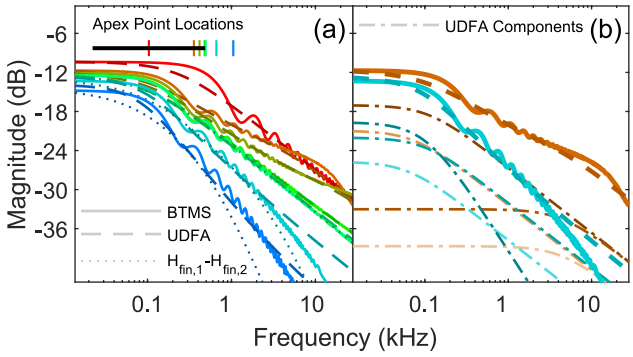

Fig. 5. (a) Transition of z_a from center of the wedge to outside the wedge. BTMS (solid), UDFA (dashed) and subtracted half wedges (dotted), in (b): Components of UDFA (dash-dotted). The black bar at the top left of (a) represents the edge, and the colored vertical bars indicate the location of the apex point. Panel (b) shows UDFA components of example apex point on (brown) and off (blue) the wedge (replotted from (a)). The darkest dash-dotted traces in b) are the $H(f_{\mathrm{c}-})$ component, whereas the brighter components are $H(f_{\mathrm{c}+})$. The off-edge component $H_{1\mathrm{st}}(f_{\mathrm{c,fin,off}})$ can be identified as the one with the steepest slope. Geometrical parameters: $L = 1.41$ m, $d_\mathrm{s} = d_\mathrm{r} = 2$ m, $\varphi = \pi/2$, $\theta_\mathrm{s} = \pi/4$, $\theta_\mathrm{b} = \pi/3$, $\theta_\mathrm{w} = 2\pi$.

the assumption in (15). At low frequencies, deviations of the underlying asymptotic filter approximation for infinite wedges from the BTMS solution result in an overestimation of the filter gain $g_{\mathrm{fin,off}}$ when late parts of the integral (14) are evaluated.

In terms of phase behavior, shown in Fig. 4(b), UDFA (dashed) follows the transition from 0° at low frequencies towards −90° (disregarding the ripples) with deviations above 100 Hz for this example of a 4 m wedge. At higher frequencies, the blended finite half wedge (see Section III-D.) causes a phase angle transition towards −45°.

D. Arbitrary Apex Point Location

To account for arbitrary apex point locations, a transition between the above two cases is required for $|z_\mathrm{a}| > L/2$ in the vicinity of the edge. When the apex point is located at one of the wedge corner points, $|z_\mathrm{a}| = L/2$, one of the two half wedges disappears and the respective gain g_{fin} of the corresponding filter becomes 0. Moving the apex point further outside the wedge results in cutting the initial part of the remaining half wedge diffraction IR (see Fig. 3(b)). Given that this underlying mechanism is not straightforwardly and efficiently implemented with filters, we propose a strongly simplified approach by blending between the remaining approximated half wedge and the above first-order filter (valid for apex points far outside the wedge). The blending function considers the initial decay of the diffraction IR, $g_{\mathrm{fin},t_{z1}}$, determined by the integral (10) up to the travelling time t_{z1} to the closer wedge corner (see right hand-side of Fig. 3), in relation to the according integral $g_{\mathrm{fin},t_{z2}}$ up to t_{z2}. In both cases, the higher cut-off frequency $f_{\mathrm{c,max}}$ of the two underlying terms with $f_{\mathrm{c}\pm,\mathrm{fin}}$ is used in (10), which dominates the initial (high frequency) decay. The diffraction IR of remaining half wedge is faded with the heuristically determined factor for which the exponent was manually adjusted to match the respective conditions in Fig. 4 (right column) and Fig. 5, as well as considering the results of the error evaluation:

$$p = \left(1 - \frac{g_{\mathrm{fin},t_{z1}}}{g_{\mathrm{fin},t_{z2}}}\right)^4, \tag{16}$$

resulting in a combined blended transfer function

$$H_{\mathrm{blend}} = p\, g_{\mathrm{fin}\pm}\, H(f_{\mathrm{c}\pm,\mathrm{fin}}) + (1-p)\, g_{\mathrm{fin,off}\pm}\, H_{1\mathrm{st}}\,(f_{\mathrm{c,fin,off}}). \tag{17}$$

Fig. 5(a) shows the effect of apex point location in relation to the wedge (indicated by the black horizontal line and the vertical, colored bars). The apex point at the center of the wedge is indicated in red, at the corner of the edge in green, and outside of the edge in blue. Intermediate locations are indicated by intermediate colors. Apex point locations inside the physical wedge (upper four traces) are described by UDFA in a physically-founded way using two half wedges according to (13) (dashed). For apex points located outside the wedge, the overall slope of the target functions (solid) transitions towards −6 dB/oct with increasing distance to the corner point of the wedge, approximated with the blending according to (16) (see lower three traces). The switch to the blending approach appears visually smooth, however, might not provide a continuous first derivative across the wedge corner point. At very high frequencies, the blended transfer function converges to a −3 dB/oct slope, deviating from the reference.

Using the (physically founded) subtraction of two half wedges each approximated by half-order low-pass filters (dotted traces) leads to considerably larger deviations than observed for the suggested blending approach. This is caused by the infinite IRs of the filter representation deviating from the underlying finite (truncated) IRs.

Fig. 5(b) illustrates the contribution of individual components (dash-dotted) to the UDFA transfer functions (dashed) for one example apex point location within the physical edge (brown) and one outside (blue), replotted from panel a). For the apex point within the edge, there are two half-order filters (dashed-dotted, red) for each of the two finite half wedges. The shorter half wedge is characterized by less gain and higher cutoff frequencies. For the apex point outside the physical edge, there are two half-order filters for the remaining half wedge (blue) and a single first-order filter for apex points far outside the edge.

IV. IIR Filter Implementation

For a computationally efficient time-domain implementation of UDFA, a recursive low-order filter design is suggested. The required first-order filters can be straightforwardly implemented as a bilinear transform design with two denominator and numerator coefficients. Modifications can be incorporated, allowing for a smooth transition to infinite cutoff frequencies and a prescribed gain at Nyquist frequency.

For the approximation of the fractional half-order filter (6) with parameters $b = 1$, $Q = 0.5$, as required for short (half) wedges, IIR design approaches exist in literature with a focus on audio applications and real-time parameter changes: A parallel low-pass filter structure was presented in [52] and an analytical design was proposed in [53]. While the latter design is optimally

suited to approximate a regular half-order low-pass filter, it cannot account for the here-required modified filter with a smoother slope transition around the cutoff frequency ($b > 1, Q < 0.5$) without numerical optimization of the filter coefficients. Since such optimization would not be feasible at run-time, a table lookup and interpolation of numerically optimized coefficients can be a solution.

Alternatively, we propose a more generally applicable, stepwise approximation of the desired modified fractional-order filters with arbitrary parameters, using a serial arrangement of first-order shelving filters and an additional overall gain factor g_{fin} for finite wedges. The knee frequencies and gains of the shelving filters are derived from the target transfer function, evaluated at equal intervals on a perceptually motivated logarithmic frequency scale. A series of two or four shelving filters, resulting in one and two second-order section (SOS) filters, respectively, was used to cover the audio frequency band up to 20 kHz, using a sampling rate f_{s} of 44.1 kHz. For a number of N shelving filters, the design range between f_{min} and f_{max} is determined by

$$f_{\text{max}} = \frac{f_{\text{s}}\, N}{4}, \tag{18}$$

where f_{max} is limited to f_{s} in case of $N > 4$, and f_{min} was chosen to be 20 Hz for $N < 3$ and 10 Hz otherwise. A number of $N - 1$ additional frequencies are determined between f_{min} and f_{max} using a logarithmic spacing, resulting in $N + 1$ frequencies $f_{\text{t,n}}$, at which the target function is evaluated resulting in target gains $g_{\text{t,n}}$. In the following, the subscript n is omitted for improved readability. The top row of Fig. 6 illustrates these sampling points (black diamonds) of the underlying UDFA target function (dashed trace) for an infinite wedge example case. Additionally, the BTMS reference (faint, thick traces in the background), and the IIR implementations are shown, with two shelving filters ($N = 2$, single SOS, left) and four shelving filters ($N = 4$, two SOS, right). First-order shelving filters of the form

$$H_{\text{sh}}(s) = \frac{1 + \sqrt{g_{\text{sh}}}\, s}{1 + s/\sqrt{g_{\text{sh}}}}, \tag{19}$$

with $s = jf/f_{\text{sh}}$ were designed using gains g_{sh} (high frequency attenuation), representing the difference of two adjacent target gains g_{t}. Based on (19), the knee frequencies f_{sh} were chosen to match the target gains g_{i} (triangles in the top row of Fig. 6) at the geometrical center frequencies f_{i} between two adjacent frequencies f_{t}:

$$f_{\text{sh}} = f_{\text{i}} \sqrt{\frac{g_{\text{d}}^2 - g_{\text{sh}}^2}{g_{\text{sh}}\,(1 - g_{\text{d}}^2)}} \left(1 + \frac{g_{\text{sh}}^2}{12}\right), \tag{20}$$

where g_{d} is the ratio of g_{i} and the previous element of gain g_{t}. The last bracketed term in (20) is an empirical correction to compensate for the overlap of the shelving filters, minimizing the deviation ($< \pm 0.2$ dB) between the target transfer function and the IIR design for four low-pass filter cutoff frequencies of 20, 200, 2000, 20000 Hz. The knee frequencies f_{sh} are shown as short black vertical bars in the top row of Fig. 6. The shelving filters (grey) are displayed together with the resulting overall magnitude response (dark, thin).

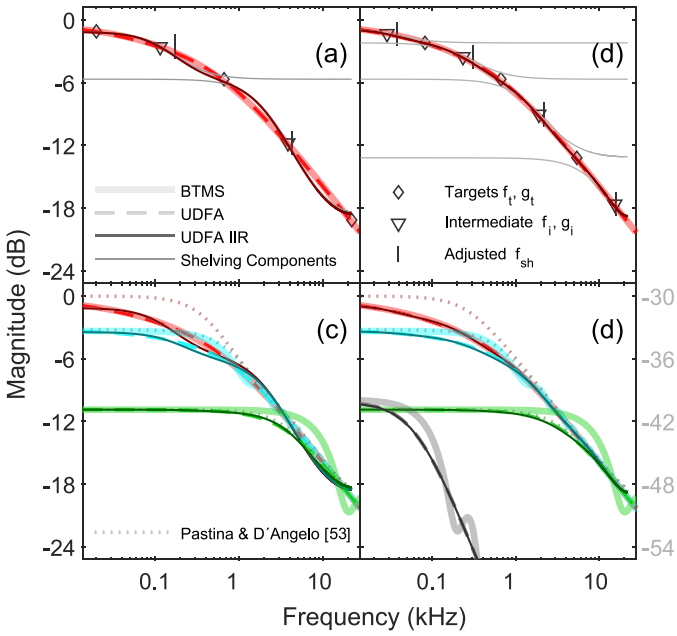

Fig. 6. Examples for the filter design. Left column: 1 SOS, right column: 2 SOS. BTMS reference (thick, solid), UDFA (dashed), and serial shelving (thin, solid, dark) magnitude response. Top row: Grey traces visualize individual shelving filters, offset by gain of previous filters for clarity. Diamonds indicate target frequencies f_{t} and gains g_{t}. Triangles indicate the intermediate frequencies f_{i} and gains g_{i}. The short vertical bars indicate the adjusted shelving frequencies f_{sh}. Bottom row: Filters for wedges of different length with geometrical parameters $\theta_{\text{b}} = \pi/6$, $d_{\text{s}} = d_{\text{r}} = 1$ m, $\varphi = \pi/2$, $\theta_{\text{s}} = 0$, $\theta_{\text{w}} = 2\pi$, $L_1 = \infty$ (red), $L_2 = 1$ m (cyan), $L_3 = 0.25$ m (green), $z_{\text{a}} = 0$ m. The approach from [54] is shown for comparison (dotted traces). The grey trace and right-hand y axis in (d) correspond to a 1 m wedge with the (virtual) apex point located outside the wedge at $z_{\text{a}} = 2$ m.

A comparison for three wedge lengths (infinite, 1 m, and 0.25 m, shown in red, cyan, and green) between the BTMS reference, UDFA, and IIR implementations with the suggested serial shelving approach and the analytical design according to [53] (dotted traces) is shown in the lower two panels of Fig. 6. In the example cases, an apex point in the center of the edge ($z_{\text{a}} = 0$) was used for clarity, such that both half wedge contributions are equal and can be summed prior to the IIR design. The additional grey traces in panel (d) illustrate the approximation for the apex point far outside the edge with a single first-order low-pass filter. For visualization purposes, a case with identical incident and reflection component is shown, while they generally have to be implemented as separate filters.

For the infinite wedge (red traces), only the serial shelving design with two SOS closely approximates the reference and will therefore be used in the following. Errors occur predominantly around the cutoff frequency for all other approaches. A combination of two shelving filters (one SOS, panel c) results in a less smooth slope. While the single SOS implementation of [53] (dotted) shows a smoother slope, the underlying unmodified fractional order filter fails to achieve the desired attenuation around the cutoff frequency for the infinite wedge (red).

The deviations between the target function and IIR implementations are less pronounced for shorter wedges (cyan, green). This can be attributed to the transition of the modified fractional

order transfer function for infinite edges to an unmodified fractional order filter for small gains g_{fin} (caused by short wedges), as implemented in (12). Hence, the analytical design [53] is suited for short wedges. The higher cutoff frequencies associated with shorter wedges also mean that the frequency response is modified in a smaller proportion of the (audio) frequency band, enabling good results even with a single SOS filter (see green traces in panel c).

The phase behavior of the IIR implementation is shown as dotted line in Fig. 4(a) and (b). At low frequencies, UDFA is closely matched, however at high frequencies, the IIR implementation converges towards a phase angle of 0° (related to the chosen design with prescribed Nyquist frequency gain). Accordingly, increasing deviations between UDFA and the IIR implementation are observed above 2 kHz.

V. Error and Computation Time Evaluation

To quantitatively evaluate the accuracy of UDFA and its IIR implementation (UDFA-IIR) in comparison to the BTMS reference, a large variety of wedges and geometrical arrangements were assessed. Source and receiver were randomly positioned in a $10 \times 10 \times 10$ m^3 cube with a uniform distribution of their Cartesian coordinates. Either a knife edge or wedge with a randomized interior angle of up to 120° ($\theta_{\text{w}} > 4\pi/3$) was centered in the cube. The wedge length was infinite or was randomly drawn between 0.2 m and 10 m. Source or receiver positions inside the wedge were excluded.[1]

To better quantify the effect of the approximations in UDFA, the geometrical arrangements have been split in knife edges and wedges, and subsequently in infinite wedges, and finite wedges with the apex point located either within ($|z_{\text{a}}| \leq L/2$) or outside ($|z_{\text{a}}| > L/2$) the physical wedge extension. Within these 3 groups, conditions were further separated in 3 zone groups (VZ, SZ, RZ). In each of the overall 18 groups, 10000 geometrical arrangements were generated (180000 in total). At 240 logarithmically-spaced frequencies between 20 Hz and 16 kHz, diffraction magnitude transfer functions were obtained for UDFA, UDFA-IIR (two SOS design) and BTMS (ED Toolbox; [54]) and normalized to the source and receiver distance over the (virtual) apex point.

Table I shows the minimum, average, and maximum Root-Mean-Square-Error (RMSE) between the BTMS reference and UDFA magnitude transfer functions. Results for the shadow and reflection zone were pooled. The Root-Mean-Square (RMS) level is shown in the top row. Additionally, the average relative error (calculated as average absolute dB deviation of the magnitude transfer functions) is provided.

As can be expected from the underlying asymptotic method, UDFA shows low average RMSEs between -40 dB and -60 dB for infinite wedges according to average relative errors smaller or equal to 0.1 dB in the shadow- and reflection zone, and average relative errors smaller than 0.5 dB in the view zone. In agreement with Section II, the errors are smaller for knife edges than for wedges with an interior angle $\theta_{\text{w}} > 4\pi/3$. The larger errors in the view zone are expected, given that the two terms in UDFA partly cancel here (also resulting in a reduced RMS). For finite wedges with the apex point inside the physical wedge, the complexity of UDFA increases (using two finite half wedges) and so does the error. Since UDFA does not account for spectral ripples caused by the truncation of the wedge impulse responses, the RMSE increases to approx. −35 dB in the shadow- and view zone, and the average relative error is up to 0.67 dB in the view zone. The largest deviations are observed for virtual apex points outside the physical wedge, where the blending of two filters in UDFA deviates from the otherwise physically-based design. Here, the average relative error is up to 5.1 dB, however, paired with an overall small diffraction term (average RMS level of −47 dB).

TABLE I
Error Measures for UDFA (Top Entry in Each Cell) and UDFA-IIR (Bottom Entry) Re the BTMS Reference. All Results are Shown in dB

		$L = \infty$		$\lvert z_{\text{a}}\rvert \leq L/2$		$\lvert z_{\text{a}}\rvert > L/2$	
		SZ RZ	VZ	SZ RZ	VZ	SZ RZ	VZ
$\theta_{\text{w}} = 2\pi$	RMS (ref.)	-10.3	-26.2	-11.6	-27.4	-27.0	-46.7
	Min. RMSE	-62.0 -56.3	-111.6 -116.7	-70.0 -70.0	-112.3 -108.2	-75.4 -79.4	-123.6 -125.5
	Avg. RMSE	-50.3 -51.1	-57.3 -61.6	-35.4 -35.0	-55.3 -53.9	-44.9 -44.7	-61.4 -61.0
	Max. RMSE	-30.1 -30.6	-47.3 -37.2	-24.2 -24.1	-34.6 -35.0	-14.4 -17.7	-22.5 -22.6
	Avg. rel. Error	0.05 0.08	0.13 0.11	0.39 0.41	0.27 0.33	2.67 2.68	3.63 3.69
$\theta_{\text{w}} > 4\pi/3$	RMS (ref.)	-10.5	-21.1	-11.7	-22.3	-28.0	-40.8
	Min. RMSE	-66.1 -59.8	-93.1 -94.6	-76.1 -76.2	-100.3 -102.2	-73.5 -74.1	-109.8 -110.0
	Avg. RMSE	-44.8 -44.9	-46.1 -46.6	-35.7 -35.2	-43.3 -42.9	-43.9 -43.9	-50.9 -50.2
	Max. RMSE	-15.6 -15.6	-16.0 -16.0	-13.5 -13.4	-19.6 -19.6	-14.1 -14.0	-17.2 -17.1
	Avg. rel. Error	0.10 0.13	0.42 0.44	0.39 0.42	0.67 0.71	3.04 3.04	5.10 5.24

For all conditions, error values for UDFA-IIR are generally close to UDFA, indicating that an implementation with 2 SOS is sufficient.

The computation time of UDFA transfer function calculation at 30 logarithmically-spaced frequencies between 20 Hz and 16 kHz, the underlying filter parameter computation and the IIR filter design were assessed in comparison to BTMS using the conditions of the above test set. In addition, UTD with the approximation proposed by Kawai [37] was added to the benchmark for infinite wedges. All computations were performed in MATLAB (R2020b) on a personal computer (Windows 10, i7-9700k CPU, 32 GB Ram). UDFA and UTD-Kawai were implemented by the authors, for BTMS the respective function of the ED Toolbox [54] was used.

Table II shows computations times in seconds required for 30000 calculations of the error evaluation cases for arbitrary wedge angles. For infinite wedges (left column), UDFA shows a large improvement over BTMS (considering a 100-m wedge as infinite) and an about two-fold reduction of computation time in

[1]To avoid potential singularity issues of BTMS [51] positions within 1.5° of zone boundaries or extensions of the wedge planes were omitted.

TABLE II
COMPUTATION TIMES IN SECONDS FOR 30000 GEOMETRICAL CONFIGURATIONS FOR INFINITE WEDGES ($L = \infty$, INCLUDING UTD-KAWAI FOR COMPARISON), AND FOR FINITE WEDGES AVERAGED OVER 30000 CONFIGURATIONS WITH APEX POINT WITHIN AND OUTSIDE THE PHYSICAL WEDGE. TRANSFER FUNCTIONS (TF) WERE EVALUATED AT 30 FREQUENCIES. FOR UDFA SEPARATE TIMES ARE PROVIDED FOR THE IIR FILTER DESIGN AND THE PARAMETER CALCULATION ALONE

	Infinite Wedge	Finite Wedge
BTMS TF	2231.6	527.16
UTD-Kawai TF	2.5587	-
UDFA TF	1.2812	2.0115
UDFA IIR Design	1.3007	1.9953
UDFA Parameters	0.2804	0.4252

comparison to UTD-Kawai (in line with two diffraction terms in UDFA compared to four terms in UTD). The IIR design is slightly slower than the transfer function calculation. The calculation of the UDFA parameters is about 10 times faster than UTD. For finite wedges (right column of Table II), the BTMS computation time shortens proportional to the now on average shorter wedge lengths and the associated number of secondary edge sources. For UDFA, computation time almost doubles, reflecting the calculation of two half wedges (instead of one for infinite wedges) or of the blending approximation. UTD is not applicable for finite wedges. The transfer function computation is at least 250 times faster than for BTMS. The computation times for the UDFA IIR design and the parameters also increase by a factor smaller than 2 in relation to the infinite edge.

VI. APPLICATION TO FLAT OBJECTS

Many real-life objects relevant in VAEs, such as door panels, boards, and tabletops, can be considered 2-dimensional flat surfaces, provided their thickness is smaller than the wavelength and they can be assumed to be rigid. The same applies for openings in walls, such as doors and windows which can be considered apertures in an infinite rigid thin screen. First-order diffraction by such objects or apertures can thus be approximated by finite knife edges representing the surface boundaries. Additional effects of higher-order diffraction will predominantly occur at low frequencies [5], [55].

Here, UDFA and UDFA-IIR (2 SOS) were applied to three basic configurations, in which flat rectangular objects act as an occluding plate (interrupting the "line-of-sight" GA direct sound path), reflector (with and without a GA specular reflection), or aperture (opening in a rigid infinite plane). Results are compared to first-order BTMS, higher-order (15th) diffraction HO-BTMS simulations computed with the ED-toolbox [54], and to measured reference data from the benchmark for room acoustics simulations (BRAS, [56]), where available. For each edge, a diffracted path was computed via the apex point either within the physical edge, or, if the (virtual) apex point was outside the physical edge, via the closer end point of the edge. The resulting diffraction paths are visualized as purple lines in the geometrical insets in Fig. 7. The contributions from each of the four finite knife edges comprising the objects were summed after distance attenuation and travel time differences were applied, corresponding to the diffracted path lengths. Depending on the configuration as occluder, reflector, or aperture, a GA contribution was added. For comparability, all diffraction functions (including the reference solution and the measurements) were normalized to the distance between the sound source and receiver via a virtual path node at the center of the diffracting object.

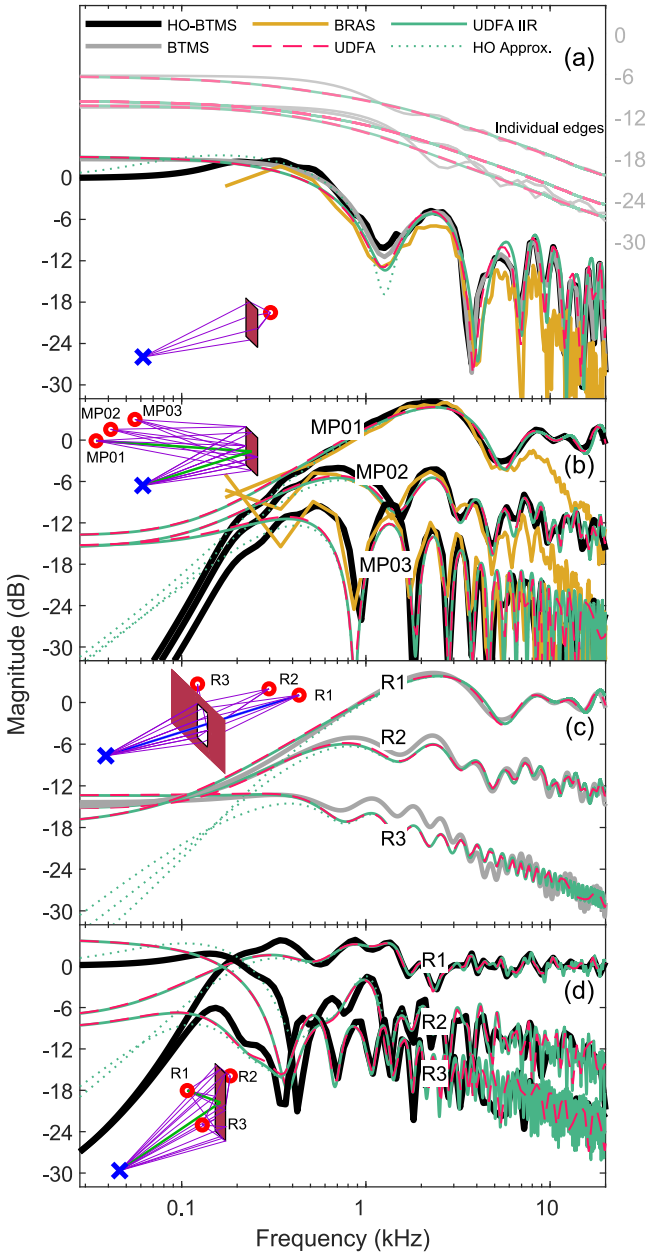

Fig. 7. Magnitude transfer functions for diffraction by a flat 1 m × 1 m rigid plate (panels a, b), aperture in a solid screen (panel c) and a 1 m × 2 m plate (panel d). BRAS measurement (solid, yellow); HO-BTMS, 15th order (solid black); BTMS (solid, grey); UDFA (dashed, pink); UDFA-IIR (solid, green); heuristic higher-order extension (dotted, green). A projection of the geometrical scenario is shown in each panel. The source is indicated as a blue cross, receiver positions are indicated by red circles. Diffraction paths are shown in purple, green lines indicate geometrical reflections, and a blue line in (c) indicates direct sound propagation following the line of sight.

A. Occluding Plate

In Fig. 7(a), we consider a flat 1 m × 1 m rigid square plate with the receiver located in the shadow zone of all edges. Given that no direct sound arrives, a comparison between measured and simulated diffraction is possible. The source is placed on a circle with a 4 m radius, centered at the middle of the plate, at an angle of 30° to the normal of the plate. The receiver is placed on a concentric circle with a radius of 1 m at an angle of 225°. An according measured transfer function with a 25 mm MDF plate in an anechoic chamber (BRAS Scene 02, LS01, MP04) is used as reference (yellow trace in Fig. 7(a)). The dashed pink and solid green traces show the (composed) UDFA and UDFA-IIR results, respectively. The grey and black solid traces show the first- and higher-order BTMS (reference) solution. Additionally, the group of (faint) traces in the top part of Fig. 7(a) shows the contributions of the individual edges, according to BTMS (grey), UDFA (dashed, pink), and the UDFA-IIR (solid, green). For better visibility, these lines are shifted upwards and use a separate scale indicated on the right.

For the overall transfer function, a good agreement of all solutions is observed, showing a general low-pass characteristic and a ripple structure. Between 200 Hz and 6 kHz, the best agreement between the measurement, (HO-) BTMS, UDFA, and the IIR implementation (solid, green) is observed. The ripples in the individual edge contributions from BTMS (top traces in Fig. 7(a)) are not represented in UDFA(-IIR), however, the main source of the well reproduced pronounced ripples in the composed transfer function are travel-time-related (linear) phase differences between the individual edge contributions (and the direct or specular reflection component in Fig. 7(b)–(d)).

At high frequencies, less energy is observed in the measurement compared to both BTMS references and the approximations, likely related to the measurement setup, absorption by the MDF panel, and effects of double diffraction at the edges of the 25 mm thick MDF plate.

At low frequencies, the comparison is restricted to BTMS: a difference is observed between HO-BTMS (black), which shows a (physically correct) unit gain at low frequencies, and UDFA (pink, dashed), which matches the (first-order) BTMS simulation (grey) with a gain of about 2 dB. These higher-order effects are addressed below in Section VI-E.

B. Reflector

In Fig. 7(b), the same 1 m × 1 m rigid square plate as above is considered, with receivers on the same side as the sound source, located in the same position as above. Results for three receiver positions at a 4 m radius at 330° (BRAS Scene 02, LS01, MP01), 315° (MP02) and 300° (MP03) are shown. Only reflected and diffracted sound are considered, and the direct sound component was removed by temporal windowing from the BRAS measurements. For MP01, a specular GA reflection exists in addition to the diffracted sound and all apex points are located on the physical edges. For MP02 and MP03, only diffracted sound is rendered and the apex point is outside the physical edge for two sides of the plate.

For MP01, a close match between all traces is observed between 200 Hz and 5 kHz. At higher frequencies, again, differences between the measurement and all simulations are observed. The simulated traces converge to a magnitude of 0 dB (also observed in Fig. 7(d), R1), which can be attributed to the geometric specular reflection contributing a dominant proportion of energy in the frequency range above the cutoff frequencies of the diffraction components.

At low frequencies, the first-order diffraction represented by UDFA(-IIR) exhibits a shelving behavior. In contrast, HO-BTMS shows a high-pass characteristic at around 100 Hz which can thus be attributed to higher-order diffraction (see Section VI-E). For MP02 and MP03, a good match is also observed between 200 Hz and 5 kHz. As for the occluding plate, the simulations overestimate the energy at high frequencies, compared to the measurements. The traces for MP02 and MP03 exhibit ripples, caused by the travel time differences between the contributions of individual wedges and an enveloping 3 dB/oct low-pass characteristic. For MP02, the diffracted sound in the mid frequencies is attenuated by about 6 dB, compared to the level of a geometrical reflection at the center point, in agreement with the observations from [57], [58]. For MP03, the attenuation effect is even stronger, as expected.

C. Aperture

Fig. 7(c) shows three receiver positions for a 1 m × 1 m aperture. The sound source is located in the same position as before. At a 4 m radius, three receiver positions are shown at 210° (R1), 225° (R2) and 255° (R3). For R1, which is a mirrored version of MP01 in the reflector case, the line of sight is unobstructed, and a direct sound GA component is rendered. For R2 (corresponding to MP02), the line of sight is just obstructed, while R3 is clearly off to the side with a larger angle in relation the plate normal than MP03. Given that BRAS does not provide measurements for an aperture and higher-order simulations for flat non-convex objects are not available in the ED-Toolbox, only first-order BTMS results are shown as a reference (grey traces).

A clear similarity between the reflector and aperture is observed, related to Babinet's principle (see, e.g., [59], Ch. 13.2). Similar to MP01 in Fig. 7(b)), superimposing GA and diffracted sound for R1 results in a shelving characteristic with ripples and convergence to 0 dB at high frequencies for both BTMS and UDFA(-IIR). For R2 (no direct sound path), all methods are in close agreement. An attenuation of about 6 dB is observed in the mid frequencies with a shallow low-pass characteristic for higher frequencies, similar to MP02 in the reflector case. For R3, all traces are similar to a half-order low-pass with spectral ripples. Here, for BTMS, an additional (low rate) ripple structure is observed, originating from the dominantly contributing finite edge itself. Given that the ripples for finite edges are not approximated by UDFA, some deviations of up to about 4 dB at 1 kHz are observed here, however, for an overall relatively small diffraction component.

D. Tilted Non-Square Plate

Fig. 7(d) shows a less symmetric arrangement with a non-square plate and source-receiver positions on a plane tilted by 39° from the horizontal plane. As before, the source is located at a distance of 4 m from the center point of the plate at an angle of

30°, here inside the tilted source-receiver plane. The receivers are placed at a shorter distance of 1 m. R1 is located at 330° with a visible geometrical reflection and R3 is located at 45° without a geometrical reflection. For R2, located at 240°, the plate acts as an occluder. HO-BTMS (black traces) serves as a reference, which is closely matched by UDFA(-IIR) above 150 Hz without accounting for higher-order diffraction effects. Minor deviations occur in the cases which do not involve a GA component (R2, R3) in the form of dense ripples at high frequencies above 3 kHz. These might be caused by differences in fine structure of the individual edge transfer functions, which are more prominent compared to the scenarios above, as the apex point for each of the paths is off-center.

E. Heuristics to Account for Higher-Order Diffraction

At low frequencies, higher-order diffraction (between the edges of the object) leads to a mismatch between UDFA and HO-BTMS. In occluded cases, the combined transfer function is overestimated at low frequencies, where unity gain occurs for higher-order simulations (e.g., Fig. 7(a), R2 in Fig. 7(d)). Otherwise, higher-order transfer functions converge towards a common high-pass characteristic with a slope of about 12 dB/oct (black traces in Fig. 7(b), R1 and R3 in Fig. 7(d)). A similar difference between simulations with only first-order diffraction and those including higher-order diffraction is shown in [55], their Fig. 2.

To approximate the spectral effects of higher-order diffraction (disregarding the exact underlying temporal effects of repeated "bounces" between the different edges in the diffraction impulse response), we propose using an additional (for simplicity first-order) high-pass filter (see green, dotted traces in Fig. 7). For rectangular reflectors, a limiting frequency f_g, above which diffraction losses at a reflector "can be considered negligible", was proposed in [57], [58]:

$$f_\mathrm{g} = \frac{cd^*}{2\,S\cos\gamma}\,, \tag{21}$$

where d^* is the characteristic distance to the reflection point, S is the surface area of the reflector and γ is the angle of incidence of the geometrical reflection on the plate (or extension thereof) in relation to the plate normal. The high-pass filter is applied to the sum of geometric reflection (where present) and diffraction with a cutoff frequency of $f_\mathrm{g}/2$. The heuristic factor $1/2$ is based on the cases covered in Fig. 7. Generally, a factor < 1 is required, given that first-order diffraction is already accounted for by UDFA, while (21) approximates the spectral effects of higher-order diffraction including first-order diffraction.

In Fig. 7(b) and for R1 and R3 in Fig. 7(d), it is observed that the resulting low-frequency behavior does not strongly depend on the receiver position, similar to the tight grouping of the HO-BTMS (black) traces at low frequencies. While the suggested (first-order) high-pass filter accounts for the main effects, the energy at low frequencies tends to be overestimated, given the steeper slope in the HO-BTMS simulations. The here suggested high-pass filtering at $f_\mathrm{g}/2$ is considered a rough approximation for objects with moderate aspects ratios for which [58] assumed that length and width "do not differ too much".

Unity gain at low frequencies for the occluded cases, observed in Fig. 7(a) and for R2 in Fig. 7(d), is achieved by rendering the high-pass filtered diffracted component, and an additional direct sound component filtered by the complementary first-order low-pass with the same cutoff frequency $f_\mathrm{g}/2$. By this, it is ensured that occluders covering only a small solid angle become "invisible" and GA occlusion is increasingly ineffective below f_g, where the wavelength is large compared to the dimensions of the object. While the proposed serial arrangement (and splitting of the frequency range) using first-order low- and high-pass filters is not physically correct, the main (spectral) effects of higher-order diffraction can be covered in a computationally efficient way.

VII. Summary and Discussion

UDFA has been introduced as a computationally highly-efficient approach to approximate edge diffraction in the framework of GA. A low-order IIR filter implementation was suggested, for which filter coefficients are generated based on target filter functions in an efficient way suited for interactive real-time updates. UDFA is applicable to the approximation of edge diffraction for all geometrical configurations including infinite and finite wedges, as well as edge-composed objects with a heuristic approach to represent higher-order diffraction. The fast computational pipeline from geometrical, physically-based parameters to filter coefficients distinguishes UDFA-IIR from earlier contributions using IIR filters, e.g., [2], where precomputing diffraction IRs from BTMS was suggested and the filter design was computationally involved, as well as from using FIR filters [18]. The IIR implementation of UDFA has the advantage that filter coefficients can be straightforwardly interpolated and updated in a delay-line-based acoustic rendering framework (e.g., [60]). Being based on an asymptotic diffraction solution, UDFA by design ensures a continuous sound field across zone boundaries. Additionally, with its underlying filter representation of diffraction, UDFA can have computational advantages compared more recent approaches based around a fast evaluation of BTMS [18], [47], when diffraction is considered for relatively long wedges and/or high frequencies and avoids singularity-issues at the (shadow- and reflection-) zone boundaries.

Depending on the target application, it is conceivable that at a given computational cost, UDFA may enable the rendering of more detailed geometry with a higher number of diffraction paths or the rendering of fewer paths with greater spectral accuracy. The accuracy which can be reached with UDFA is scalable and can be adapted by increasing the number of underlying terms in the filter representation to four [50] or by increasing or decreasing the number of filter coefficients in the IIR implementation.

A prominent feature of UDFA is the validity in all three zones including the view and reflection zone, whereas some earlier approaches [16], [48] only considered the shadow zone. Additionally, when only considering the shadow zone, the current (most efficient) single-term solution for infinite wedges

can also be applied for finite wedges (including a DC gain), resulting in a close approximation for sufficiently large bending angles, while also converging to a flat response with unity gain at the shadow boundary. By this, UDFA enables highly efficient, simplified rendering of finite edges, reducing inaccuracies at low frequencies as reported by [36], where the infinite wedge UTD solution was used.

Modeling diffraction by non-rigid wedges, as is often required in noise control, may be feasible with UDFA if the boundary conditions are accounted for in the underlying analytical approach. In principle this is possible in UTD [26], which has been also expressed in a filter representation [50] that can serve as a basis for UDFA.

A. Relation Between UDFA and Existing Analytical Solutions

The suggested (two-term) UDFA is based on the filter representation of diffraction described in [50], which is in turn derived from the asymptotic solution of [27], [29] for infinite wedges. The filter representation can be considered exact when compared to the underlying asymptotic solution, except for deviations in the range of ± 0.1 dB caused by the fractional-order filter representation (6). For infinite wedges, the asymptotic solution itself has limitations at low frequencies and at positions of source or receiver close to the edge, particularly in the view zone. Nevertheless, deviations of UDFA compared to the BTMS reference remain small for infinite edges (see Table I, left). Using a filter approach with four components (based on UTD or BTMS) as described in [50] would further improve accuracy, and particularly expand applicability of UDFA to a wider range of wedge angles including $\theta_\mathrm{w} < 4\pi/3$.

For finite wedges with apex point within the physical wedge, the finite (truncated) half wedge diffraction IRs are approximated by infinite diffraction IRs, hence neglecting ripples in the magnitude transfer function. Accordingly, deviations to BTMS increase (see Table I, middle), however, UDFA parameters are still clearly physically-based.

For finite wedges with the apex point located outside the physical wedge, UDFA omits the underlying mechanism of subtraction of two truncated half wedge diffraction IRs and blends in a first-order diffraction filter representing the response far outside the physical wedge. This simplification leads to increased deviations from BTMS (see Table I, right). Here, using four terms could improve accuracy for the integral-derived gains (10), (14).

While it is important to be aware of the limitations imposed by the asymptotic solution and the simplifications in UDFA, they might not be the bottleneck in terms of precision in VAE applications. The current evaluation with composed objects already showed that effects of higher-order diffraction dominate deviations at low frequencies.

B. Composed Objects

In the application case of composed flat objects, depending on the geometrical configuration, deviations between UDFA and BTMS of up to 4 dB occur around the cutoff frequency. While such deviations are likely perceptually detectable in a direct comparison using broadband noise stimuli (e.g., [61]), perceptual effects in the context of VAE are less clear. Recently, [62] investigated the perceived naturalness of several low-complexity diffraction models for single-wedge diffraction in static and dynamic scenarios. Models that omitted spectral ripples/comb filtering received favorable ratings in terms of naturalness when compared to BTMS. [63] investigated detection thresholds of spectral ripples, using speech and 1.2 ripples per octave, in the context of different room acoustic conditions and in the presence of interfering sounds. They report detection thresholds of between 6.1 dB and 7.2 dB peak-to-valley ratio. Generally, the perceptual salience of spectral deviations depends on many factors such as the source signal and the frequency range in which they occur (e.g., [64]). [65] have used a minimum peak-to-valley ratio of 5 dB for their spectral ripples to assess perceived naturalness of spectrally distorted speech and music. Further investigations of perceptual differences are required with regard to perceptual plausibility and authenticity in static and dynamic VAEs, particularly for diffraction by finite objects.

The current test cases demonstrate the relevance of the relative delay and the basic low-pass characteristic of the response from the individual edges to account for the prominent (large scale) ripple structure in the overall transfer functions for objects. The capability of representing these ripples distinguishes UDFA from, e.g., the smooth spectra achieved by the recent volumetric diffraction and transmission approach ([19], their Fig. 13).

Although the representation of flat objects by a combination of finite edges disregards effects of not perfectly rigid and not non-absorbing real-life objects, deviations from the measured transfer functions from BRAS were mainly prevalent at high frequencies, where an overall attenuation of both the approximated and measured sound might likely lead to a reduced perceptual salience of the differences.

Overall, UDFA offers a close spectral approximation for diffraction from flat objects and apertures for most of the human hearing range, enabling the efficient incorporation of numerous objects into a VAE, such as doors, tables, and reflectors in concert venues.

C. Higher-Order Diffraction

One area for future extensions is higher-order diffraction. At low frequencies, effects of higher-order diffraction were prominent for the current finite objects, as observed in the difference between the first- and higher-order BTMS simulations (see also [5], [55], [58]). The proposed heuristic "higher-order compensation" filter approach helps to avoid considerable low-frequency errors that would otherwise occur, e.g., in the shadow zone of small and distant objects. With restricting diffraction effects to an according high-pass band it is ensured that objects covering only a small solid angle from both the source's and receiver's perspective "disappear". Future improvements may include increased accuracy and strategies to handle three-dimensional objects.

Higher-order diffraction also needs to be considered for diffraction around multiple room corners or around three-dimensional objects, such as a rectangular column, where sound can only reach the shadow zone via double diffraction. Here,

UDFA would be applied to a series of diffraction nodes (see e.g., [18], [36]). For computational efficiency, is conceivable that for flat objects, the current simplification using knife edges could be extended by a further low-pass component mimicking effects of double diffraction at high frequencies when the thickness of the flat object with respect to the wavelength becomes relevant (for the 25 mm MDF plate measured in BRAS: above about 10 kHz).

D. Computational Efficiency

The suggested UDFA approach enables a fast estimation of the energetic contribution of sound propagation paths, doubling performance re UTD (with Kawai approximation) for infinite edges and reducing computation time by a factor of at least 250 for finite wedges re BTMS. Given that the path finding is a major factor for computational costs, particularly in detailed scenes [15], [36], energetic and perceptually motivated path culling at early stages is desirable. As for an entire scene, the number of rendered paths for a finite object that may be reduced by prioritizing paths with a dominant energetic contribution [66]. A potential application of UDFA is to determine gains for parametric filter banks as used in [36]. In addition to low computation times, UDFA has the advantage of being applicable to finite wedges (in contrast to, e.g., UTD), avoiding excessive low-frequency errors.

An implementation of UDFA as recursive filters has been proposed based on a serial shelving filter approach with scalable complexity. The implementation with two SOS filters closely approximates the target functions and in the case of composed objects leads to overall transfer functions (green traces, Fig. 7) that are virtually identical to the UDFA result (dashed, pink traces, Fig. 7). Computation times for the UDFA filter coefficients are similar to evaluating the transfer function for a 30-band third-octave parametric filter bank. Further reductions in computational complexity can likely be achieved with parallel arrangements of low-pass filters (e.g., [52]) or using the proposed serial shelving approach to approximate either the sum of both the shadow- and reflection component or even the sum of two half wedges. As a further simplification, the target diffraction function for an entire object can be derived using UDFA and approximated by a single filter (see, e.g., [49] for a machine learning based approach). The computation time for the underlying UDFA parameters is exceptionally low (see bottom row of Table II).

VIII. Conclusion

A universal, physically-based approach to approximate first-order diffraction by infinite and finite wedges and by objects composed thereof has been suggested, using a computationally-efficient filter representation. UDFA offers simple-to-derive parameters of diffraction low-pass filter functions, implemented as low-order IIR filters with scalable precision. The BTMS reference simulation and measured transfer functions can be well matched by combining the approximated diffraction functions of the individual edges of flat rectangular rigid objects, constituting an important group of objects in VAE, like tables or door openings. To approximate prominent effects of higher-order diffraction observed at low frequencies for such objects, an additional heuristically motivated high-pass and complementary low-pass filter have been proposed. The following conclusions can be drawn:

- Spectral characteristics of diffraction from infinite and finite wedges can be approximated by a combination of modified fractional- and first-order low-pass filters.
- The proposed serial shelving IIR implementation closely approximates the target transfer functions in the audio-frequency range using two SOS filters.
- Measurements of diffraction from flat objects can be matched in a wide frequency range. The low-pass characteristic and the travel-time delay of the contributions from the underlying individual edges are most relevant for the resulting diffraction magnitude response.
- The accuracy and computational cost of UDFA is scalable. Depending on the application, a single filter can be used, implemented in a single SOS, while for highest accuracy, each contributing half wedge can be composed of multiple filter components.

Appendix A
Relation of Cutoff Frequencies

The impulse response of a finite half wedge is a truncated version of the impulse response of an infinite half wedge. When the apex point is located within the physical wedge, the onset of the impulse response remains unchanged and accordingly the truncated half wedge transfer function converges to the that of the infinite half wedge at high frequencies. With

$$\lim_{f\to\infty}\left((jf/f_\mathrm{c})+1\right)^{-\alpha}=\left((jf/f_\mathrm{c})\right)^{-\alpha}, \tag{23}$$

and assuming a cutoff frequency $f_{\mathrm{c,fin}}$ and a gain g_{fin} for the finite half wedge, the two converging asymptotic transfer functions are

$$g_{\mathrm{fin}}\left((jf/f_{\mathrm{c,fin}})\right)^{-\alpha}=\left((jf/f_\mathrm{c})\right)^{-\alpha}, \tag{24}$$

resulting in the relation

$$f_{\mathrm{c,\ fin}}=\frac{1}{g_{\mathrm{fin}}^{\frac{1}{\alpha}}}f_\mathrm{c}, \tag{25}$$

which is equivalent to (11) with $\alpha=1/2$.

Appendix B
Cutoff Frequency for Rectangular Window

The approximation of wedge diffraction with an apex point located outside the physical wedge by a first-order low-pass filter (III.C) is based on the assumption that the travel time difference around both corner points $\Delta t=(t_2-t_1)$ is comparatively short, leading to a truncated edge impulse that is converging towards a rectangular function. With $\mathrm{sinc}\,(x)=\sin(\pi x)/(\pi x)$, the magnitude frequency response $|H_\mathrm{r}(f)|$ of such rectangular function with amplitude 1 and duration Δt is

$$|H_\mathrm{r}(f)|=|\mathrm{sinc}(\Delta t f)|\,. \tag{26}$$

By choice, a cutoff frequency $f_{\mathrm{c,fin,off}}$ of a first-order low-filter is determined, such that the slope of its magnitude transfer function is a tangent to the extrema of $|H_{\mathrm{r}}(f)|$.

The locations of the extrema x_n of the sinc-function are non-trivial to describe analytically, however, for large positive arguments, they converge towards the extrema of the sine function

$$x_n = \frac{1}{2} + n, \tag{27}$$

where n are positive integers at the location of maxima of $|H_{\mathrm{r}}(f)|$. To obtain an expression for the cutoff frequency $f_{\mathrm{c,fin,off}}$ that approximately fulfills the chosen criteria, the following equation has to be solved for $f_{\mathrm{c,fin,off}}$ at $f = x_n/\Delta t$:

$$\left| \left(\frac{j x_n/\Delta t}{f_{\mathrm{c,fin,off}}} + 1 \right)^{-1} \right| = |\mathrm{sinc}(x_n)| \tag{28}$$

Assuming $x_n/\Delta t \gg f_{\mathrm{c,fin,off}}$, the equation becomes more manageable and can be solved for $f_{\mathrm{c,fin,off}}$:

$$f_{\mathrm{c,fin,off}} = \left| \frac{j\, x_n\, \mathrm{sinc}(x_n)}{\Delta t} \right| = \left| \frac{j\, \sin(\pi x_n)}{\pi\, \Delta t} \right| . \tag{29}$$

For large n, according to (27), the sine in (29) becomes ± 1, yielding (15).

ACKNOWLEDGMENT

The authors would like to thank U. Peter Svensson for insightful discussions and his edge diffraction (ED) toolbox.

REFERENCES

[1] P. Menounou and V. Asimakopoulos, "Empirical formulas for predicting the insertion loss behind wedges," *Appl. Acoust.*, vol. 182, Nov. 2021, Art. no. 108166.
[2] T. Lokki, U. P. Svensson, and L. Savioja, "An efficient auralization of edge diffraction," in *Proc. Audio Eng. Soc. 21st Int. Conf.*, 2002, pp. 166–172.
[3] R. Torres, M. Kleiner, and B.-I. Dalenbäck, "Audibility of 'diffusion' in room acoustics auralization: An initial investigation," *Acta Acustica United Acustica*, vol. 86, pp. 919–927, Nov. 2000.
[4] R. R. Torres, U. P. Svensson, and M. Kleiner, "Computation of edge diffraction for more accurate room acoustics auralization," *J. Acoust. Soc. Amer.*, vol. 109, no. 2, pp. 600–610, Feb. 2001.
[5] R. Torres, N. Rycker, and M. Kleiner, "Edge diffraction and surface scattering in concert halls: Physical and perceptual aspects," *J. Temporal Des. Architecture Environ.*, vol. 4, no. 1, pp. 52–58, Jan. 2004.
[6] J. Rindel, "The use of computer modeling in room acoustics," *J. Vibroengineering*, vol. 3, no. 4, pp. 219–224, Feb. 2001.
[7] B. B. Boren, "Acoustic simulation of J.S. Bach's Thomaskirche in 1723 and 1539," *Acta Acust*, vol. 5, 2021, Art. no. 14.
[8] L. Aspöck et al., "Application of virtual acoustic environments in the scope of auditory research," in *Proc. XXVIII Encontro Sociedade Brasileira Acústica*, 2018, doi: 10.17648/sobrac-87162.
[9] M. Cord, D. Baskent, S. Kalluri, and B. Moore, "Disparity between clinical assessment and real-world performance of hearing aids," *Hear. Rev.*, vol. 14, pp. 22–26, 2007.
[10] J. Jerger, "Ecologically valid measures of hearing aid performance," *Starkey Audiology Ser.*, vol. 1, no. 1, pp. 1–4, 2009.
[11] F. Brinkmann, L. Aspöck, D. Ackermann, S. Lepa, M. Vorländer, and S. Weinzierl, "A round robin on room acoustical simulation and auralization," *J. Acoust. Soc. Amer.*, vol. 145, no. 4, pp. 2746–2760, Apr. 2019.
[12] J. B. Allen and D. A. Berkley, "Image method for efficiently simulating small-room acoustics," *J. Acoust. Soc. Amer.*, vol. 65, no. 4, pp. 943–950, Apr. 1979.
[13] J. Borish, "Extension of the image model to arbitrary polyhedra," *J. Acoustical Soc. Amer.*, vol. 75, no. 6, pp. 1827–1836, Jun. 1984.
[14] T. Wendt, S. van de Par, and S. Ewert, "A computationally-efficient and perceptually-plausible algorithm for binaural room impulse response simulation," *J. Audio Eng. Soc.*, vol. 62, no. 11, pp. 748–766, Dec. 2014.
[15] A. Erraji, J. Stienen, and M. Vorländer, "The image edge model," *Acta Acustica*, vol. 5, 2021, Art. no. 17.
[16] N. Tsingos, T. Funkhouser, A. Ngan, and I. Carlbom, "Modeling acoustics in virtual environments using the uniform theory of diffraction," in *Proc. 28th Annu. Conf. Comput. Graph. Interactive Techn.*, 2001, pp. 545–552.
[17] T. Funkhouser et al., "A beam tracing method for interactive architectural acoustics," *J. Acoust. Soc. Amer.*, vol. 115, no. 2, pp. 739–756, Jan. 2004.
[18] D. Schröder, "Physically based real-time auralization of interactive virtual environments," Ph.D. dissertation, RWTH Aachen, Logos Verlag, Berlin, Germany, 2011.
[19] L. Pisha, S. Atre, J. Burnett, and S. Yadegari, "Approximate diffraction modeling for real-time sound propagation simulation," *J. Acoust. Soc. Amer.*, vol. 148, no. 4, pp. 1922–1933, Oct. 2020.
[20] A. Sommerfeld, "Mathematische theorie der diffraction," *Mathematische Annalen*, vol. 47, no. 2, pp. 317–374, Jun. 1896.
[21] G. D. Malyuzhinets, "Excitation, reflection and emission of surface waves from a wedge with given face impedances," *Sov. Phys. Doklady*, vol. 3, pp. 752–755, 1958.
[22] J. B. Keller, "Geometrical theory of diffraction," *J. Opt. Soc. Amer.*, vol. 52, no. 2, pp. 116–130, Feb. 1962.
[23] B. Lu, M. Darmon, C. Potel, and V. Zernov, "Models Comparison for the scattering of an acoustic wave on immersed targets," *J. Phys.: Conf. Ser.*, vol. 353, Mar. 2012, Art. no. 012009.
[24] M. A. Nethercote, R. C. Assier, and I. D. Abrahams, "Analytical methods for perfect wedge diffraction: A review," *Wave Motion*, vol. 93, Mar. 2020, Art. no. 102479.
[25] S.-W. Lee and G. Deschamps, "A uniform asymptotic theory of electromagnetic diffraction by a curved wedge," *IEEE Trans. Antennas Propag.*, vol. 24, no. 1, pp. 25–34, Jan. 1976.
[26] R. G. Kouyoumjian and P. H. Pathak, "A uniform geometrical theory of diffraction for an edge in a perfectly conducting surface," *Proc. IEEE*, vol. 62, no. 11, pp. 1448–1461, Nov. 1974.
[27] A. D. Pierce, "Diffraction of sound around corners and over wide barriers," *J. Acoust. Soc. Amer.*, vol. 55, no. 5, pp. 941–955, May 1974.
[28] W. J. Hadden and A. D. Pierce, "Sound diffraction around screens and wedges for arbitrary point source locations," *J. Acoustical Soc. Amer.*, vol. 69, no. 5, pp. 1266–1276, May 1981.
[29] A. D. Pierce, *Acoustics: An Introduction to its Physical Principles and Applications*. Berlin, Germany: Springer, 2019.
[30] W. J. Hadden Jr. and A. D. Pierce, "Diffraction of sound by nearly rigid barriers," *Adv. Eng. Sci.*, vol. 3, pp. 1009–1018, 1976.
[31] P. Y. Ufimtsev, "Method of edge waves in the physical theory of diffraction," (from the Russian 'metod krayevykh voln v fizicheskoy teorii difraktsii' *Izd-Vo Sov. Radio*, pp. 1–243, 1962), translated by the U.S. Air Force Foreign Technology Division, 1971. [Online]. Available: https://apps.dtic.mil/sti/citations/AD0733203
[32] P. Y. Ufimtsev, *Fundamentals of the Physical Theory of Diffraction*. Hoboken, NJ, USA: Wiley, 2007.
[33] F. Hacivelioglu, L. Sevgi, and P. Y. Ufimtsev, "Electromagnetic wave scattering from a wedge with perfectly reflecting boundaries: Analysis of asymptotic techniques," *IEEE Antennas Propag. Mag.*, vol. 53, no. 3, pp. 232–253, Jun. 2011.
[34] R. Tiberio and S. Maci, "An incremental theory of diffraction: Scalar formulation," *IEEE Trans. Antennas Propag.*, vol. 42, no. 5, pp. 600–612, May 1994.
[35] M. Darmon, A. K. Djakou, S. Chehade, C. Potel, and L. Fradkin, "Two elastodynamic incremental models: The incremental theory of diffraction and a huygens method," *IEEE Trans. Ultrason., Ferroelect., Freq. Control*, vol. 66, no. 5, pp. 998–1005, May 2019.
[36] C. Schissler, G. Mückl, and P. Calamia, "Fast diffraction pathfinding for dynamic sound propagation," *Assoc. Comput. Machinery Trans. Graph.*, vol. 40, no. 4, pp. 1–13, Aug. 2021.
[37] T. Kawai, "Sound diffraction by a many-sided barrier or pillar," *J. Sound Vib.*, vol. 79, no. 2, pp. 229–242, Nov. 1981.
[38] Z. Maekawa, "Noise reduction by screens," *Appl. Acoust.*, vol. 1, no. 3, pp. 157–173, Jul. 1968.
[39] P. Menounou, I. J. Busch-Vishniac, and D. T. Blackstock, "Directive line source model: A new model for sound diffraction by half planes and wedges," *J. Acoust. Soc. Amer.*, vol. 107, no. 6, pp. 2973–2986, Jun. 2000.

[40] P. Menounou and P. Nikolaou, "An extension to the directive line source model for diffraction by half planes and wedges," *Acta Acustica United Acustica*, vol. 102, no. 2, pp. 307–321, Mar. 2016.
[41] U. P. Svensson, R. I. Fred, and J. Vanderkooy, "An analytic secondary source model of edge diffraction impulse responses," *J. Acoust. Soc. Amer.*, vol. 106, no. 5, pp. 2331–2344, Oct. 1999.
[42] U. P. Svensson, P. T. Calamia, and S. Nakanishi, "Frequency-domain edge diffraction for finite and infinite edges," *Acta Acustica, United Acust*, vol. 95, no. 3, pp. 568–572, May 2009.
[43] M. A. Biot and I. Tolstoy, "Formulation of wave propagation in infinite media by normal coordinates with an application to diffraction," *J. Acoust. Soc. Amer.*, vol. 29, no. 3, pp. 381–391, Mar. 1957.
[44] H. Medwin, "Shadowing by finite noise barriers," *J. Acoust. Soc. Amer.*, vol. 69, no. 4, pp. 1060–1064, Apr. 1981.
[45] A. Asheim and U. P. Svensson, "An integral equation formulation for the diffraction from convex plates and polyhedra," *J. Acoust. Soc. Amer.*, vol. 133, no. 6, pp. 3681–3691, Jun. 2013.
[46] P. T. Calamia and U. P. Svensson, "Edge subdivision for fast diffraction calculations," in *Proc. IEEE Workshop Appl. Signal Process. Audio Acoust.*, 2005, pp. 187–190.
[47] P. T. Calamia and U. P. Svensson, "Fast time-domain edge-diffraction calculations for interactive acoustic simulations," *Eur. Assoc. Signal Process. J. Adv. Signal Process.*, vol. 2007, pp. 1–10, Dec. 2006.
[48] C. Kirsch and S. D. Ewert, "Low-order filter approximation of diffraction for virtual acoustics," in *Proc. IEEE Workshop Appl. Signal Process. Audio Acoust.*, 2021, pp. 341–345.
[49] V. Pulkki and U. P. Svensson, "Machine-learning-based estimation and rendering of scattering in virtual reality," *J. Acoust. Soc. Amer.*, vol. 145, no. 4, pp. 2664–2676, Apr. 2019.
[50] S. D. Ewert, "A filter representation of diffraction at infinite and finite wedges," *J. Acoust. Soc. Amer. Exp. Lett.*, vol. 2, no. 9, Sep. 2022, Art. no. 092401.
[51] U. P. Svensson, "Edge-diffraction impulse responses near specular-zone and shadow-zone boundaries," *Acta Acustica United Acustica*, vol. 92, pp. 501–512, 2006.
[52] T. Hélie, "Simulation of fractional-order low-pass filters," *IEEE/Assoc. Comput. Machinery Trans. Audio Speech Lang. Process.*, vol. 22, no. 11, pp. 1636–1647, Nov. 2014.
[53] P. P. L. Pastina and S. D'Angelo, "Optimal integer order approximation of fractional order filters," in *Proc. IEEE 23rd Int. Conf. Digit. Audio Effects*, 2021, pp. 89–96.
[54] U. P. Svensson, "ED toolbox," 2018, Accessed: Feb. 1, 2023. [Online]. Available: https://github.com/upsvensson/Edge-diffraction-Matlab-toolbox
[55] U. P. Svensson, S. R. Martin, J. Šlechta, J. E. Summers, B. H. Teres, and C. F. Gaumond, "Accuracy aspects for diffraction-based computation of scattering," in *Proc. Euronoise Crete*, 2018, pp. 2093–2098.
[56] L. Aspöck, F. Brinkmann, D. Ackermann, S. Weinzierl, and M. Vorländer, *BRAS - Benchmark for Room Acoustical Simulation*. Berlin, Germany: TU Berlin, 2020, doi: 10.14279/DEPOSITONCE-6726.3.
[57] J. Rindel, "Attenuation of sound reflections due to diffraction," in *Proc. Nordic Acoustical Meeting*, 1986, pp. 257–260.
[58] J. H. Rindel, "Acoustic design of reflectors in auditoria," *Proc. Inst. Acoust.*, vol. 14, no. 2, pp. 119–129, 1992.
[59] L. L. Beranek and T. Mellow, *Acoustics*. Amsterdam, The Netherlands: Elsevier, 2013.
[60] L. Savioja, J. Huopaniemi, T. Lokki, and R. Väänänen, "Creating interactive virtual acoustic environments," *J. Audio Eng. Soc.*, vol. 47, pp. 675–705, Sep. 1999.
[61] F. Toole and S. E. Olive, "The modification of timbre by resonances: Perception and measurement," *J. Audio Eng. Soc.*, vol. 36, no. 3, pp. 122–142, Mar. 1988.
[62] J. Mannall, O. Das, P. Calamia, and E. De Sena, "Perceptual evaluation of low-complexity diffraction models from a single edge," in *Proc. Audio Eng. Soc. Int. Audio Virtual Augmented Reality Conf.*, 2022.
[63] T. Biberger and S. D. Ewert, "Binaural detection thresholds and audio quality of speech and music signals in complex acoustic environments," *Front. Psychol.*, vol. 13, Nov. 2022, Art. no. 994047.
[64] R. Bücklein, "Hörbarkeit von Unregelmäßigkeiten in Frequenzgängen bei akustischer Übertragung' (detection of irregularities in the frequency responses of acoustic transmissions)," in *Elektroakustik II. Nachrichtentechnische Fachberichte*, vol. 26, J. Wosnik, Ed. Wiesbaden, Germany: Vieweg+Teubner Verlag, 1962, pp. 42–47.
[65] B. C. J. Moore and C.-T. Tan, "Perceived naturalness of spectrally distorted speech and music," *J. Acoust. Soc. Amer.*, vol. 114, no. 1, pp. 408–419, Jul. 2003.
[66] P. T. Calamia and U. P. Svensson, "Culling insignificant diffraction components for interactive acoustic simulations," in *Proc. 19th Int. Congr. Acoust.*, Madrid, Spain, 2007, pp. 2573–2578.

Christoph Kirsch studied media and acoustical engineering in Mittweida, Germany, and received the master's degree in signal processing and acoustics from Aalborg University, Aalborg, Denmark, in 2019. He is currently working toward the Ph.D. degree at Carl von Ossietzky Universität, Oldenburg, Germany. His work is focused on efficient techniques for perceptually plausible acoustic rendering. His contribution regarding rendering and requirements on the spatial resolution of late reverberation was the recipient of the Best Student Paper Award at the International Conference on Immersive and 3D Audio 2021.

Stephan D. Ewert studied physics and received the Ph.D. degree from the Carl von Ossietzky Universität Oldenburg, Germany, in 2002. During his Ph.D. project, he spent a 3-month stay as a Visiting Scientist with the Research Lab of Electronics, Massachusetts Institute of Technology, Cambridge, MA, USA. From 2003 to 2005, he was an Assistant Professor with the Centre of Applied Hearing Research, Technical University of Denmark, Lyngby, Denmark. In 2005, he re-joined Medizinische Physik at the Universität Oldenburg, where he has been the Head of the Psychoacoustic and Auditory Modeling Group since 2008. His field of expertise is psychoacoustics and acoustics with a strong emphasis on perceptual models of hearing and virtual acoustics. He has authored various papers on spectro-temporal processing, binaural hearing, and speech intelligibility. He also focused on perceptual consequences of hearing loss, hearing-aid algorithms, instrumental audio quality prediction, and room acoustics simulation.